

Gaussian process modeling of heterogeneity and discontinuities using Voronoi tessellations

Christopher A. Pope*, John Paul Gosling, Stuart Barber,
School of Mathematics, University of Leeds,
Jill Johnson,

School of Earth and Environment, University of Leeds,
Takanobu Yamaguchi, Graham Feingold,
Chemical Sciences Division, Earth System Research Laboratory,
National Ocean and Atmospheric Administration, Boulder, CO 80305

and

Paul G. Blackwell,
School of Mathematics and Statistics, University of Sheffield.

February 28, 2022

Abstract

Many methods for modelling functions over high-dimensional spaces assume global smoothness properties; such assumptions are often violated in practice. We introduce a method for modelling functions that display heterogeneity or contain discontinuities. The heterogeneity is dealt with by using a combination of Voronoi tessellation, to partition the input space, and separate Gaussian processes to model the function over different regions of the partitioned space. The proposed method is highly flexible since it allows the Voronoi cells to combine to form regions, which enables non-convex and disconnected regions to be considered. In such problems, identifying the borders between regions is often of great importance and we propose an adaptive sampling method to gain extra information along such borders. The method is illustrated by simulated examples and an application to real data, in which we see improvements in prediction error over the commonly used stationary Gaussian process and other non-stationary variations. In our application, a computationally expensive computer model that simulates the formation of clouds is investigated, the proposed method more accurately predicts the underlying process at unobserved locations than existing emulation methods.

Keywords: emulation, Gaussian process, locating discontinuities, Voronoi tessellation.

*The first author gratefully acknowledges the financial support of the John E Crowther – Martin Clarke Research Foundation.

1 INTRODUCTION

Many methods used to model uncertainty about functions make assumptions about the smoothness of the function over its input space. By smoothness, we are referring to the assumption that minor perturbations in the inputs lead to only minor changes in the function’s output. However, there are many examples of small fluctuations in the input causing great changes in a function’s output. We discuss one such example in Section 6, where small changes in the input parameters of a computer model of a cloud formation process lead to large changes in the properties of the process. Naively modelling these functions using methods that rely on the assumption of smoothness can lead to poor results when the models are used for analysis such as prediction (Paciorek and Schervish, 2006). Methods which make fewer smoothness assumptions, such as mixtures of thin plate splines (Wood et al., 2002), local linear regression (Cleveland et al., 1992) and wavelet-based imputation (Heaton and Silverman, 2008), have been used to build approximations for the underlying functions of these processes. By making so few assumptions about the data, methods such as these have the drawback that a large number of observations are needed to build an accurate model of the underlying process. We propose an approach where the space is divided into disjoint regions such that the process can be assumed to be smooth within each region, while allowing for abrupt changes at the boundaries of the regions. Within each region, the local smoothness assumption means that the model can function with relatively few data points. The method in this paper is applicable to many situations where a process displays heterogeneity or discontinuities separating regions that are internally smooth.

One well-established method for spatial modelling is Gaussian process regression or kriging (Cressie, 1993; Handcock and Stein, 1993). By using a Gaussian process to model the underlying function, we are making an assumption of smoothness in the underlying function over the entire input space. As mentioned previously, this assumption is rarely justified. To deal with this, adaptations to the stationary Gaussian process methodology must be made to accommodate non-stationarity. Two of the main methods that have been focused on in the literature are changes to the covariance function, such as spatial deformations (Sampson and Guttorp, 1992; Schmidt and O’Hagan, 2003) or convolution based methods (Higdon, 1998; Risser and Calder, 2015), and the use of independent Gaussian processes over a partitioned space, such as treed Gaussian process (TGP; Gramacy and Lee, 2008) or piecewise Gaussian process (PGP; Kim et al., 2005). This paper’s focus is the latter of the two categories, and readers interested in adaptations to the covariance function are directed to Risser (2016) for a review.

In order to fit a piecewise Gaussian process model, we must specify a technique for partitioning the input space. Both of the methods mentioned previously partition the input space to give regions with straight boundaries: treed partitioning does so using non-overlapping lines parallel to the input

axes and Voronoi tessellation uses the Euclidean distance from a set of centres to create Voronoi cells. In this paper, we shall focus on partitioning the input space using Voronoi tessellation due to its flexibility compared to treed partitioning. We allow Voronoi cells to join together to create larger, more flexible, joint regions. Once we have specified the partition of the input space, we can fit separate Gaussian processes to each region. The models which are built using Voronoi tessellations in Kim et al. (2005) are a special case of this where there is no combining of cells and severe constraints are applied to the locations of the centres. The joining of tessellation cells allows more complex regions, such as when one region is surrounded by another, or non-convex shaped regions, without the loss of information that is intrinsic to building regions that can only be a single independent cell. Very importantly, we also look to allow a greater range of models than the PGP model of Kim et al. (2005) by changing the prior distribution of the centres that defines the cells of the tessellation.

We also tackle the problem of adaptive sampling where the aim is to locate the discontinuities in the function and major changes in the function’s response to inputs. This gives us a means of reducing uncertainty about the regions’ boundaries via further sampling. Traditional sampling methods are not geared towards this objective and are shown by examples to perform worse than the proposed method in the presence of different regions.

Our application, the System for Atmospheric Modelling (SAM) model (Khairoutdinov and Randall, 2003) is very computationally expensive, a single run taking over ten hours, and so the model behaviour over the six-dimensional parameter space cannot be fully explored using it directly. Hence, the proposed approach to generate a statistical representation of the model provides a means by which the cloud behaviour can be more rigorously examined. The clouds that the SAM model simulates are particularly sensitive to aerosol concentrations in the atmosphere and meteorological conditions, where small changes in temperature and humidity profiles can impact strongly on whether clouds form or not, and how thick/reflective they are. The proposed statistical method, which does not assume global smoothness, allows us to represent and explore the SAM model more accurately than existing methods.

We give a brief overview of the stationary Gaussian process model in Section 2. In Section 3, we describe the proposed partitioning technique and the MCMC methods needed to remove dependence on the partition structure for inference. Section 4 introduces an adaptive sampling method used to better define the location of a discontinuity. Section 5 demonstrates the technique on a simulated example, and Section 6 shows the method applied to a real example. We finish with a discussion of the method and possible future extensions in Section 7.

2 MODELLING USING A GAUSSIAN PROCESS

We consider a measured attribute $y \in \mathbb{R}$ corresponding to inputs $\mathbf{x} \in \mathcal{X} \subseteq \mathbb{R}^d$. In a spatial setting, \mathbf{x} corresponds to the spatial location; however, we are not restricted to this, and more general high-dimensional inputs can be used for other applications in analysing computer model output. We represent the relationship between the input and output by a function: $y = \eta(\mathbf{x})$. The output y is not necessarily a scalar, though we only consider the case of a scalar output in this paper. Examples of multivariate outputs are given by Rougier (2008), Fricker et al. (2013) and Conti and O'Hagan (2010); the proposed approach could be extended for multivariate outputs. Spatial process data are typically measured with natural variation or error, so repeated observations of identical \mathbf{x} results in different outputs y . The approach we propose is also applicable to cases in which the output is deterministic, where multiple applications of the same \mathbf{x} will result in the same output y , which is often found when considering computer model output, such as those seen in Sacks et al. (1989), Linkletter et al. (2006) and Currin et al. (1991). In this paper, we employ the Gaussian process as a regression model; however, this is just one possible choice and other statistical models could be used.

The conditional mean of $\eta(\mathbf{x})$ given a vector of coefficients $\boldsymbol{\beta}$ is given by

$$E\{\eta(\mathbf{x})|\boldsymbol{\beta}\} = \mathbf{h}(\mathbf{x})^T \boldsymbol{\beta}.$$

The vector $\mathbf{h}(\cdot)$ consists of q known regression functions of \mathbf{x} , incorporating any beliefs that we might have about the form of $\eta(\cdot)$. In this paper, we use a constant function to illustrate the methodology. The covariance between $\eta(\mathbf{x})$ and $\eta(\mathbf{x}')$ is given by

$$\text{cov}(\eta(\mathbf{x}), \eta(\mathbf{x}') | \sigma^2, B, \sigma_\epsilon^2) = \sigma^2 c(\mathbf{x}, \mathbf{x}' | B) + \sigma_\epsilon^2 \delta_{\mathbf{x}'\mathbf{x}},$$

conditionally on σ^2 , σ_ϵ^2 and B , where $c(\mathbf{x}, \mathbf{x}' | B)$ is a correlation function that depends on parameters given in B , σ^2 is a scaling term for the covariance, σ_ϵ^2 is an error or nugget term and $\delta_{\mathbf{x}'\mathbf{x}}$ is a Kronecker delta which is one if and only if $\mathbf{x}' = \mathbf{x}$ and zero otherwise. The function $c(\cdot, \cdot | B)$ must ensure that the covariance matrix of any set of inputs is positive semidefinite. A common choice for this function is the Gaussian correlation function

$$c(\mathbf{x}, \mathbf{x}' | B) = \exp \left\{ -(\mathbf{x} - \mathbf{x}')^T B (\mathbf{x} - \mathbf{x}') \right\},$$

where B is a diagonal matrix of roughness parameters. In this paper, we shall simply estimate values of B and σ_ϵ^2 using optimisation techniques on the likelihood.

The output of $\eta(\cdot)$ is observed at n locations, $\mathbf{X} = \{\mathbf{x}_1, \dots, \mathbf{x}_n\}$, to obtain data \mathbf{y} . We denote

the collection of n observed inputs and outputs as training data $\mathbf{D} = ((\mathbf{x}_1, y_1), \dots, (\mathbf{x}_n, y_n))^T$. The likelihood of the data given the parameters can be seen in O'Hagan (1992) to be

$$L(B, \sigma_\epsilon^2; \mathbf{D}) \propto |A|^{-\frac{1}{2}} |H^T A^{-1} H|^{-\frac{1}{2}} (\hat{\sigma}^2)^{\frac{q-n}{2}},$$

where

$$\begin{aligned} H^T &= (\mathbf{h}(\mathbf{x}_1)^T, \dots, \mathbf{h}(\mathbf{x}_n)^T), \\ A_{ij} &= c(\mathbf{x}_i, \mathbf{x}_j | B) + \sigma_\epsilon^2 \delta_{ij}, \\ \hat{\sigma}^2 &= \frac{\mathbf{y}^T (A^{-1} - A^{-1} H (H^T A^{-1} H)^{-1} H^T A^{-1}) \mathbf{y}}{n - q - 2}. \end{aligned} \tag{1}$$

If we have data in which the output is deterministic, we set $\sigma_\epsilon = 0$, so $A_{ij} = c(\mathbf{x}_i, \mathbf{x}_j | B)$. We use a weak prior $p(\sigma^2, \beta) \propto \sigma^{-2}$ for the other hyperparameters as given in O'Hagan (1992). Alternatively, more informative priors can be used if there are stronger beliefs about the parameters (Oakley, 2002).

From properties of the multivariate normal distribution, O'Hagan (1992) has shown that

$$\left. \frac{\eta(\mathbf{x}) - m^*(\mathbf{x})}{\hat{\sigma} \left(\frac{n-q-2}{n-q} c^*(\mathbf{x}, \mathbf{x} | B) \right)^{\frac{1}{2}}} \right| \mathbf{D}, B, \sigma_\epsilon^2 \sim t_{n-q},$$

where

$$\begin{aligned} m^*(\mathbf{x}) &= \mathbf{h}(\mathbf{x})^T \hat{\beta} + \mathbf{v}(\mathbf{x})^T A^{-1} (\mathbf{y} - H \hat{\beta}), \\ c^*(\mathbf{x}, \mathbf{x}') &= c(\mathbf{x}, \mathbf{x}' | B) - \mathbf{v}(\mathbf{x})^T A^{-1} \mathbf{v}(\mathbf{x}) \\ &\quad + (\mathbf{h}(\mathbf{x})^T - \mathbf{v}(\mathbf{x})^T A^{-1} H) (H^T A^{-1} H)^{-1} (\mathbf{h}(\mathbf{x})^T - \mathbf{v}(\mathbf{x})^T A^{-1} H)^T, \\ \mathbf{v}(\mathbf{x})^T &= (c(\mathbf{x}, \mathbf{x}_1 | B), \dots, c(\mathbf{x}, \mathbf{x}_n | B)), \\ \hat{\beta} &= (H^T A^{-1} H)^{-1} H^T A^{-1} \mathbf{y}. \end{aligned} \tag{2}$$

Equation (2) shows that the posterior mean, $m^*(\mathbf{x})$, is based on the maximum a posteriori (MAP) estimate of the mean function from the prior, adjusted for on how close the point is to other training points.

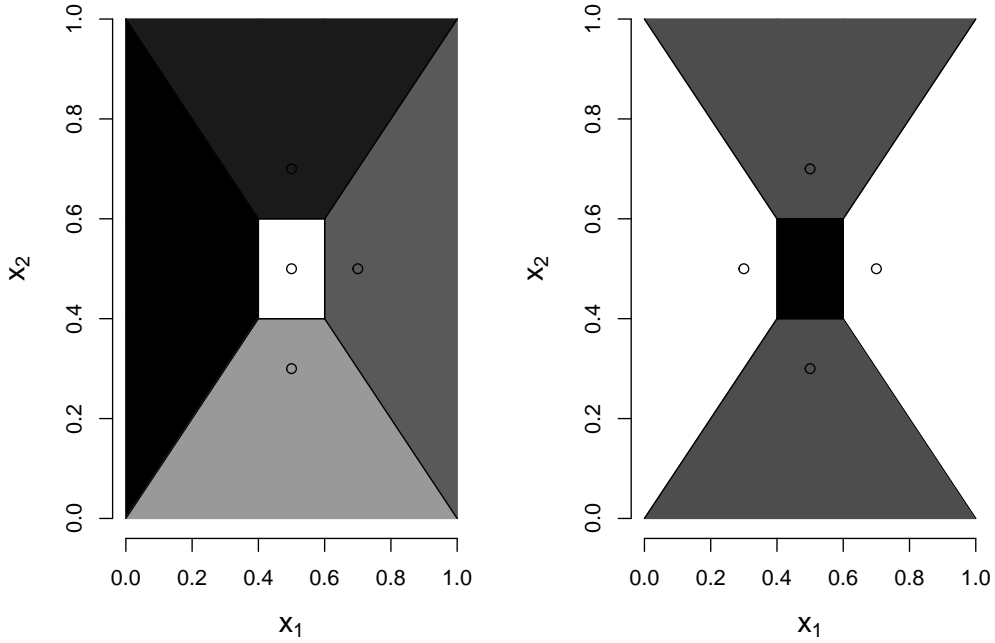


Figure 1: Possible regions formed from a Voronoi tessellation, using a simple two dimensional example with five centres. Regions are indicated by shading tone. Left: All cells are independent, forming five regions with one cell in each region. Right: Cells combine to form three regions. The left and right cells combine to form one region, as do the top and bottom cells.

3 PIECEWISE GAUSSIAN PROCESS PRIOR

3.1 Voronoi tessellation with joint centres

We allow for discontinuities in the value of $\eta(\cdot)$ by partitioning the input space \mathcal{X} into r disjoint regions R_1, \dots, R_r and denote this partition by $\mathbf{R} = \{R_1, \dots, R_r\}$. The partition structure that we employ is based on a Voronoi tessellation. A standard Voronoi tessellation is defined by a set of k centres, $\mathbf{x}_T^* = \{\mathbf{x}_{T_1}^*, \dots, \mathbf{x}_{T_k}^*\}$. An arbitrary point $\mathbf{x} \in \mathcal{X}$ is contained in the cell of the i th centre $\mathbf{x}_{T_i}^*$ if

$$d(\mathbf{x}, \mathbf{x}_{T_i}^*) < d(\mathbf{x}, \mathbf{x}_{T_j}^*) \quad \forall j \in \{1, \dots, k\} \setminus i,$$

where $d(\mathbf{x}, \mathbf{x}_{T_j}^*)$ is the Euclidean distance between \mathbf{x} and $\mathbf{x}_{T_j}^*$. If we have a finite number of unique, disjoint centres in finite-dimensional Euclidean space, all of the Voronoi cells are convex polytopes (Gallier, 2008).

To allow for more flexibility than a standard Voronoi tessellation, each region R_i consists of one

or more Voronoi cells. We do not require Voronoi cells to be neighbours to be in the same region. Hence a region R_i need not be contiguous or convex, unlike the underlying Voronoi cells. Also, note that we do not restrict the centres to be the training points \mathbf{x}_i

A simple example of a possible tessellation of $\mathcal{X} = [0, 1]^2$ can be seen in Figure 1. On the left is a Voronoi tessellation of five cells. On the right, the top and bottom cells have joined to form one region, as have the left and right cells; cells in the same region have the same shading.

The proposed tessellation differs from that used in the PGP method of Kim et al. (2005) in two important ways. Kim et al. (2005) require the centres to be at data points; deciding which data points to used as centres is a key part of fitting a PGP model. Moreover, all cells are treated independently in the sense that a separate Gaussian process is built in each cell. To see why using only Voronoi cells centred on the data points is limiting, consider an input space that is made up of two different functions on two regions which form a partition of the input space. We would ideally want to model this using two separate Gaussian processes, one on each region. This can only be modelled accurately using the PGP method if the two regions divide the input space in a way that can be modelled using just two Voronoi cells, each centred on one of the existing data points.

We could still attempt to model a setup such as this using the PGP method with a larger number of independent centres. However, there are two clear drawbacks to doing so. First, by splitting a region into multiple independent cells, we are not using all of the points from that region to estimate the parameters of the Gaussian process, namely $\beta, B, \sigma_\epsilon^2$ and σ^2 . By using a single region, as allowed for in the proposed approach, all points from the region can be utilized simultaneously to gain better parameter estimates. Secondly, using a weak prior distribution for the GP parameters has the constraint that we need at least four points to build a Gaussian process with a defined variance, which could make accurately modelling a function with a discontinuity impossible. We may, for example, only have five points sampled in a given region and may not be able to model this region with one centre, making it inadvisable to split this into multiple regions.

However, this flexibility does come at a price; there are potential identifiability issues in the proposed approach due to the flexibility of defining the regions. A single region which consists of multiple cells joined together can be equivalent to a region in another model consisting of a single cell. This could be easily addressed by putting a proper prior distribution on the number of cells, k , since the two models will have different number of underlying Voronoi cells.

We refer to the partition of the k Voronoi cells into r regions as a set of *relationships* between the cells. In Figure 1 above, the relationship is that the top and bottom cells form one region, the left and right cells form a second region, and lastly the centre cell forms a region. Define \mathcal{C} to be a space such that each element of \mathcal{C} is one of the possible relationships between the k centres, then $c \in \mathcal{C}$ is an index of which relationship is used.

We denote the collection of tessellation parameters by $\mathbf{t} = \{\mathbf{x}_T^*, k, r, c\}$ and assign the priors

$$\begin{aligned}\pi(\mathbf{t}) &= \pi(k, \mathbf{x}_T^*)\pi(r|k)\pi(c|k), \\ k, \mathbf{x}_T^* &\sim \text{PoiPr}(\lambda), \\ r|k &\sim DU(1, k), \\ c|k &\sim DU(1, b_k)\end{aligned}$$

to model the partition of the input space. Here $\text{PoiPr}(\lambda)$ is a Poisson process with intensity parameter λ , $DU(1, k)$ is a discrete uniform distribution on $\{1, \dots, k\}$, and the k th Bell number b_k is the number of all possible ordered partitions (Aigner, 1999). It should be noted that λ is the only hyperparameter that needs choosing. Typically, λ is chosen by trialling different values until a suitable model is found; alternatively, we could place a prior distribution on it. There are many adjustments that could be made to incorporate prior beliefs about the underlying model. For example, one adjustment that could be made if appropriate is to replace the Poisson process by one that includes a repulsion term, such as a Gibbs process (Illian et al., 2008). Using a repulsion term would have the benefit of additional centres having a localised effect on the model tessellation, but in all examples we have studied, we have found the Poisson process to work well.

Combining the separate Gaussian processes on the different regions yields the likelihood

$$L(\mathbf{t}, \mathbf{B}, \boldsymbol{\beta}, \sigma^2, \sigma_\epsilon^2; \mathbf{D}) \propto \prod_{i=1}^r f_i(\mathbf{y}_i | \mathbf{x}_i, B_i, \sigma_i^2, \sigma_\epsilon^2, \boldsymbol{\beta}_i, \mathbf{t}),$$

where $f_i(\mathbf{y}_i | \mathbf{x}_i, B_i, \sigma_i^2, \sigma_\epsilon^2, \boldsymbol{\beta}_i, \mathbf{t})$ is the multivariate Gaussian distribution for outputs \mathbf{y}_i corresponding to inputs \mathbf{x}_i which lie in the i th region. We can analytically integrate over $\boldsymbol{\beta}$ and σ^2 to give the posterior distribution

$$\pi(\mathbf{B}, \mathbf{t}, \sigma_\epsilon^2 | \mathbf{D}) \propto \prod_{i=1}^r |H_i^T A_i^{-1} H_i|^{-\frac{1}{2}} |A_i|^{-\frac{1}{2}} \Gamma\left(\frac{n_i - q}{2}\right) \left[\frac{2}{(n_i - q - 2)\hat{\sigma}_i^2} \right]^{\frac{(n_i - q)}{2}},$$

where n_i is the number of data points in the i th region, $\Gamma(\cdot)$ is the gamma function and H_i , A_i and $\hat{\sigma}_i^2$ are as defined in (1), with the subscript i showing that these terms are evaluated using the points that lie in the i th region.

The posterior distribution for \mathbf{B} and σ_ϵ^2 is analytically intractable, and we select the parameter values by maximising the likelihood of the B_i for each region and σ_ϵ^2 . Alternatively, we could take uncertainty in these parameters into account by placing proper prior distributions on them and including them within the MCMC method; however, this has been found to have minimal impact on the resulting predictions and associated uncertainty (for example, see Abt, 1999; Nagy et al., 2007).

3.2 MCMC implementation

We use reversible-jump MCMC (RJMCMC) (Green, 1995) to estimate the posterior distributions of the model parameters. We require different move types to accommodate the model elements to update: the set of centres for the tessellation and the relationship between the centres. To update the set of centres, we add, take away, or move a centre: these moves are called *birth*, *death* and *move* respectively. To update the relationship between the centres we change a single centre to be in a different region, possibly a new region with no other centre; this move is called *change*. This gives us four possible general moves.

Algorithm 1 The RJMCMC implementation of the Joint centre Voronoi Gaussian process

```

Begin with a random valid tessellation  $\mathbf{t}_0$ ;
for  $i = 1, \dots, n_s$  do
  Propose Birth, Death, Move or Change with equal probability;
  if Birth proposed then
     $\mathbf{x}_{T(k+1)}^* = P; P \sim U_k(\mathbf{0}, \mathbf{1})$ ;
    Update  $c$  such that  $\mathbf{x}_{T(k+1)}^*$  is combined with an existing region or forms a new region;
  else if Death proposed then
    Remove one element of  $\mathbf{x}_T^*$  at random;
    Remove the chosen point's relationship in  $c$ ;
  else if Move proposed then
    Select an element of  $\mathbf{x}_T^*$  at random,  $\mathbf{x}_{T_j}^*$  say;
    Propose a new centre  $P \sim N_k(\mathbf{x}_{T_j}^*, \Sigma_p)$ , with  $\Sigma_p$  tuned for mixing;
    Set  $\mathbf{x}_{T_j}^* = P$ ;
  else if Change proposed then
    Select an element of  $\mathbf{x}_T^*$  at random,  $\mathbf{x}_{T_j}^*$  say;
    Change  $\mathbf{x}_{T_j}^*$ 's relationship in  $c$  s.t. it is independent or related to a different region;
  end if
  Update the current tessellation  $\mathbf{t}_i$  to obtain proposed tessellation  $\mathbf{t}_p$ ;
  Fit an independent Gaussian process to each region in  $\mathbf{t}_p$ ;
  Choose  $B$  and  $\sigma_\epsilon^2$  to be the values that maximise the likelihood (2);
  Calculate the posterior of the proposed model  $\pi(\mathbf{B}, \mathbf{t}_p, \sigma_\epsilon^2 | \mathbf{D})$ ;
  Generate  $U_i \sim U[0, 1]$ ;
  if  $U_i \leq \frac{\pi(\mathbf{B}, \mathbf{t}_p, \sigma_\epsilon^2 | \mathbf{D})}{\pi(\mathbf{B}, \mathbf{t}_i, \sigma_\epsilon^2 | \mathbf{D})} \times \text{Prior ratio} \times \text{Adjustment}$  then
     $\mathbf{t}_i = \mathbf{t}_p$ ;
  else
     $\mathbf{t}_i = \mathbf{t}_{i-1}$ ;
  end if
end for

```

These four types of proposal are taken to be equally likely during the proposal step. We use an acceptance ratio that is the same as that described in Green (1995), which has the form

$$\alpha = \min(1, \text{Likelihood ratio} \times \text{Prior ratio} \times \text{Proposal ratio}).$$

Due to the setup of the moves, we find that the acceptance ratio simplifies to the ratio of the

likelihood of the proposed model to that of the existing model. As we cannot have a death when we have one centre and we also cannot change the relationship of the centre, we only propose birth and move steps in that situation. To maintain reversibility here, when a birth step is proposed, we multiply the acceptance ratio by $1/2$, and, conversely, we multiply the acceptance ratio by 2 when we have two centres and we propose a death step. These multiplications are called adjustments, and we set the adjustment to 1 in all other cases. Pseudo-code detailing the RJMCMC implementation is given in Algorithm 1.

After the RJMCMC update of the tessellation, we fit independent Gaussian processes to each region. We can then use the Gaussian process model on each region to make predictions at points in the same region.

4 ADAPTIVE SAMPLING TO IDENTIFY DISCONTINUITIES

In some applications, it may be possible to gather additional data at new training points \mathbf{x}^* . In many cases, this is costly and/or time consuming, so these values of \mathbf{x}^* must be chosen with care. Some applications, such as the cloud modelling we discuss in Section 6, have a number of regions separated by discontinuities and one region is of particular interest. In such cases, learning more about both that region’s boundary and the surface close to the boundary can be of great importance. In particular, we may wish to sample additional design points close to the boundary such that we estimate any discontinuities or borders between regions more accurately. Having more information around the discontinuity will not only help us predict outcome values at unobserved locations with more accuracy, but will also supplement the understanding we have about where the discontinuities are occurring, which is often of practical interest. Common sampling methods such as space-filling algorithms and largest uncertainty samplers (Santner et al., 2003) are not tailored to this objective, and adaptive samplers for Gaussian processes have other objectives like reducing overall error or reducing uncertainty (Williams et al., 2000; Loepky et al., 2010).

We propose the following sampling method to help estimate these boundaries. The approximate MAP model is found by looking at which tessellation in the posterior sample has the largest likelihood value. The method looks at the MAP model and samples points on the boundary of the region of interest in this model, which is taken to be a good estimate of the boundary of the discontinuity. There are an infinite number of positions that we could sample on the boundary, and so we attempt to maximise the information we get from each sample. We iteratively choose points on this boundary that are furthest from all existing design points to try to attain some of the properties that are established for space-filling designs. Pseudo-code for this sampling method is given in Algorithm 2.

We note that it would be straightforward to extend this sampling method to sample on the boundary of any region or multiple regions. A change could be made to the algorithm if we are able to double the number of points that we can sample. Instead of sampling at a point $\tilde{\mathbf{x}}_j$, we could look at the line that interpolates $\tilde{\mathbf{x}}_j$ and the centre of its corresponding cell \mathbf{x}_{T_i} , then sample two points on this line at distances $\|\tilde{\mathbf{x}}_j - \mathbf{x}_{T_i}\| \pm \epsilon$ from the centre. That is, rather than sampling at the point $\tilde{\mathbf{x}}_j$, we sample at points $\tilde{\mathbf{x}}_j \pm \epsilon|\mathbf{x}_{T_i} - \tilde{\mathbf{x}}_j|$, where $0 < \epsilon \ll 1$. This adaptation should in theory sample just inside and just outside of the discontinuity if ϵ is chosen suitably. It would also be straightforward to adjust this sampling approach to generate points on or near boundaries giving preference to points with higher posterior uncertainty if we wished to improve both boundary detection and function estimates.

Algorithm 2 The boundary sampling method

Require: $n_p > 0$ — number of points to sample;

Require: \mathbf{X} — the n locations with observed data;

Require: \mathbf{y} — the n outputs corresponding to locations \mathbf{X} ;

Implement the method from Section 3.1 to gain a posterior sample of models;

Find the MAP model from these posterior samples;

Identify the region whose boundary is to be investigated;

Randomly sample a candidate set of $n^* \gg n_p$ points $\tilde{\mathbf{X}}$ on the boundary of the region;

for $k = 1, \dots, n_p$ **do**

 Select the point $\tilde{\mathbf{x}}_i$ such that

$$i = \operatorname{argmax}_{i \in 1, \dots, n^*} \min_{j \in 1, \dots, n} d(\tilde{\mathbf{x}}_i, \mathbf{x}_j);$$

 Remove $\tilde{\mathbf{x}}_i$ from $\tilde{\mathbf{X}}$ and add it to \mathbf{X} ;

 Update $n \leftarrow n + 1$;

end for

Sample outputs $\eta(\cdot)$ at locations $\{\mathbf{x}_{n+1}, \dots, \mathbf{x}_{n+n_p}\}$.

5 ILLUSTRATIVE EXAMPLES

5.1 A diamond-shaped discontinuity

To initially test the proposed modelling approach, we apply it to the deterministic test function shown in Figure 2. The example has a discontinuity defined by straight lines, but these are not parallel to the parameter axes. The function is defined by

$$\eta_1(\mathbf{x}) = \begin{cases} \sin(x_1) + \cos(x_2) & \text{for } \mathbf{x} \in T, \\ \sin(x_1) + \cos(x_2) + 10 & \text{else,} \end{cases}$$

where $T = \{\mathbf{x} : x_2 - x_1 \leq 0.2 \cap x_2 - x_1 \geq -0.2 \cap x_2 + x_1 \geq 0.8 \cap x_2 + x_1 \leq 1.2\}$.

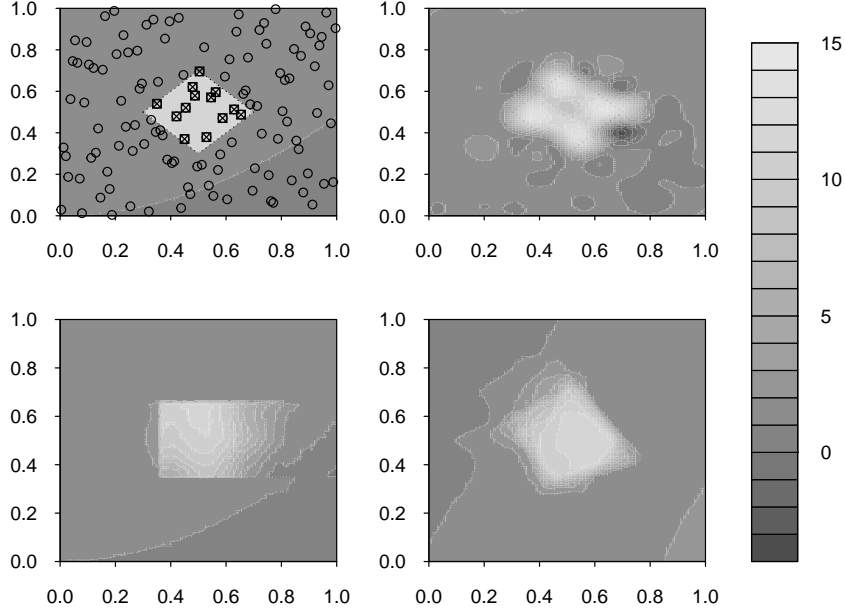


Figure 2: Top left: The true diamond test function and design points used; design points within the discontinuity are square and those outside are shown as circles. Top right: The standard Gaussian process mean surface. Bottom left: The TGP integrated surface. Bottom right: The integrated surface of the proposed method.

We evaluate the function at 80 design points, chosen using a Latin hypercube design with a maximin criterion to get a good coverage of the input space (Johnson et al., 1990). One thing of interest here is to inspect the surface estimate produced by the proposed model and how this compares to the true surface. Due to the nature of the posterior samples, any estimated surface obtained from a single sample would be conditional on the tessellation \mathbf{t}_i for that sample. We can numerically integrate over \mathbf{t} via Monte Carlo methods using the posterior sample and, hence, have an integrated mean surface that is not conditional on the tessellation parameter; that is an estimate of $E_{\mathbf{t}}(E_{\eta(\cdot)}(\cdot))$. This will be referred to as the *integrated surface* whilst the surface of a single sample will be referred to as a *mean surface*. To create the integrated surface, we find the value of the mean surface for each of the posterior tessellation samples at 10,000 points, using an equispaced grid of 100×100 points, and find the pointwise mean of these surface over the samples.

We compare different analysis methods using the mean squared error (MSE) of the integrated surface for each method. We find that the MSE of the proposed method ($\text{MSE} = 1.84$) is smaller than that of both the Treed GP ($\text{MSE} = 1.98$) and the standard GP ($\text{MSE} = 2.04$). The MSE of the proposed method compared to the others suggests that the new approach is more representative of the true surface. The integrated surfaces of all of the methods can be seen in Figure 2. We also

note that it performs better than the convolution based Gaussian process ($\text{MSE} = 2.13$).

We also consider the performance of the adaptive sampler for this example. The MAP model from the posterior sample is shown in Figure 3. The MAP model has 14 cells divided into two regions, with one region containing 12 of these cells and the other region containing just two. The region with two cells, which contains all of the points from inside the discontinuity, is the region whose boundary we will sample on. To do this, we implement the sampler from Algorithm 2, using 2000 candidate points on the boundary and selecting five of these points to evaluate and include in the training data.

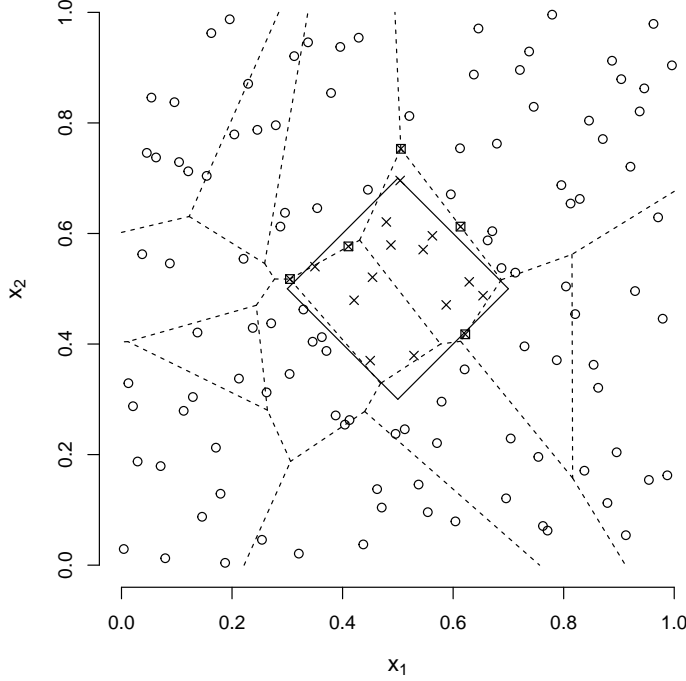


Figure 3: MAP tessellation of the diamond example, with the true discontinuity shown as a solid line. Circles and crosses show design points outside and inside the discontinuity respectively. Cell boundaries from the approximate MAP model are shown as dashed lines. The two cells containing all the discontinuity design points form one region and the remaining cells form a second region. New design points selected by the adaptive sampler algorithm are denoted by crossed squares.

	Number of regions						
	1	2	3	4	5	6	7
Original points	0.000	0.294	0.505	0.118	0.047	0.023	0.014
After sampler	0.000	0.595	0.280	0.060	0.021	0.031	0.006

Table 1: Posterior probabilities for the number of regions in the diamond example before and after the adaptive sampler was used.

We can see in Figure 3 that two of the points we have chosen to sample lie very close to the true discontinuity, and, around those areas, we should have a much better understanding about the

location of the boundary. We will also reduce the uncertainty about the mean function around the other three points that have been sampled although these points do not lie as close to the boundary as the two previously mentioned. We compare the proposed adaptive sampling method to two existing methods of selecting new design points: using a Sobol sequence (Giunta et al., 2003) and selecting the points in \mathcal{X} that have the largest posterior variance. We find that the adaptive sampling algorithm produces the smallest MSE (MSE = 1.352) using the method from section 4 when an additional five points are sampled compared to using Sobel (MSE = 1.511) and the largest posterior uncertainty (MSE = 1.392). Table 1 reports the posterior probability of r regions for $r = 1, \dots, 7$ using the proposed method on the original 80 design points and on the 85 points including those chosen by the adaptive sampler. The most probable number of regions is not equal to the true number of regions when only the original points are considered. However, the true number of regions becomes the most probable when the additional new points are added. In fact, as we further sample more points, we become more confident that the number of regions is two ($\Pr(r = 2) = 0.89$ when we sample an additional 10 points using the adaptive sampler).

5.2 A discontinuity with curved boundaries

The second test function, shown in Figure 4a, is a particularly difficult one as precisely representing a circular boundary using Voronoi tessellation would need an infinite number of centres. This test function is defined as

$$\eta_2(\mathbf{x}) = \begin{cases} x_1^2 + 5x_2^2 + 3 \cos(10x_1^2 + 5x_2^2) + 10 & \text{for } \mathbf{x} \in L, \\ x_1^2 + 5x_2^2 + 3 \cos(10x_1^2 + 5x_2^2) & \text{else,} \end{cases}$$

where

$$L = \{\mathbf{x} : \{x_1 \in [0.25, 0.6] \cup x_2 \in [0.3, 0.6]\} \cup \{(x_1 - 0.25)^2 + (x_2 - 0.6)^2 \leq 0.15^2\} \\ \cup \{(x_1 - 0.6)^2 + (x_2 - 0.6)^2 \leq 0.15^2\} \cap \{(x_1 - 0.4125)^2 + (x_2 - 0.3)^2 \leq 0.175^2\}\}.$$

We evaluate the function at 70 design points chosen using a Latin square design with a maximin criterion to ensure even coverage of the input space (Johnson et al., 1990). The integrated surface obtained by the proposed method can be seen in Figure 4b. We can see that the method has performed as well as can be expected when considering the data we have used to train it. The mean squared error of the integrated surface for the proposed method (MSE = 4.498) is lower than that for the TGP (MSE = 6.886) or the standard GP (MSE = 6.473).

In the TGP method, the input space is partitioned using non-overlapping straight lines parallel to the parameter axes and a separate Gaussian process is built for each region. We can see from

the shape of L in Figure 4a that we would need a large number of these regions to be able to get a good approximation for the true shape of the discontinuity. A similar argument follows when we consider the shape of T in the simulated example of Section 5.1. Since a standard GP is inappropriate for both of these functions due the smoothness assumption clearly being violated. As a result the mean function must over-smooth to ensure that the function intersects the training points exactly leading to poor estimates around the discontinuity, leading to high MSE values.

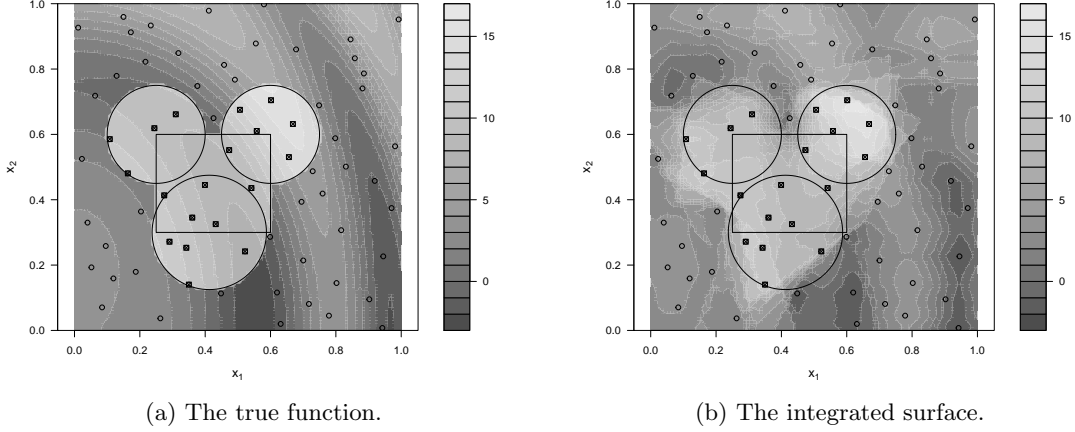


Figure 4: Filled contour plots of the true function from equation (5.2) and the integrated surface of the proposed method.

6 APPLICATION: Cloud modelling

We illustrate the proposed method on simulation data from a complex numerical cloud-resolving model, the System for Atmospheric Modelling (SAM) (Khairoutdinov and Randall, 2003). For this example, the model is used to simulate the development of shallow nocturnal marine stratocumulus clouds for 12 hours over a domain of size 40 km x 40 km x 1.5 km height. Initial conditions are described through a vector \mathbf{x} of six key parameters. These simulations are an updated version of the nocturnal marine stratocumulus simulations (set 2) described in detail in Feingold et al. (2016), with longer run-time and updated radiation scheme. We focus here on the average predicted cloud coverage fraction over the domain in the final hour of the simulations, y .

Shallow clouds are very important to the climate system as they reflect solar energy to space and hence cool the planet, offsetting some of the greenhouse gas warming. These clouds are particularly sensitive to aerosol concentrations in the atmosphere and meteorological conditions, where small changes in temperature and humidity profiles can impact strongly on whether clouds form or not, and how thick/reflective they are. It is essential to understand how changes in aerosol and meteorological conditions can affect shallow clouds in order to improve their representation in climate models.

Currently, large-scale climate model representations of shallow clouds are poor as they form and develop on smaller scales than the large grids used, yet how they are represented can have a strong influence on predictions of climate sensitivity, in particular the magnitude of warming for a prescribed increase in CO₂.

Initial investigations of these SAM simulations and expert opinion has suggested that the model potentially produces two different forms of cloud behaviour, open and closed cell behaviour, over the six-dimensional parameter space. Hence, the underlying function we wish to model is potentially made up of a single function with two regimes, likely containing a discontinuity in y as the model behaviour moves between these regimes. As such, there is also interest in knowing about the location of any discontinuity/change in regime in order to explore where and why this phenomenon occurs.

We have 105 training points available from the simulations to model the cloud coverage fraction, y , where the input combinations were chosen to cover the 6-d parameter space using a space-filling maximin Latin hypercube design. The six parameters investigated here are listed in Table 2, and scatter plots of the outputs against the individual inputs can be seen in Figure 5, in which there is clear evidence of two regimes but no obvious way of splitting the data according to a single input parameter. We see from Figure 5 that most areas of the parameter space output consistent values of y at around 0.9; however, some other areas have much smaller values of y , from 0.2 to 0.4. The plot of the output against the aerosol concentration (x_6) input suggests that high values of this variable are very likely to yield large cloud coverage values; however, there is no clear way to differentiate low values.

Label	Input description	Range investigated
x_1	Liquid water potential temperature	284–294 K
x_2	Total non-precipitating water mixing ratio	6.5–10.5 g·kg ^{−1}
x_3	Depth of mixing layer	500–1300 m
x_4	Jump in water potential temperature at inversion	6–10 K
x_5	Jump in water mixing ratio at inversion	6–10 g·kg ^{−1}
x_6	Aerosol concentration	30–500 cm ^{−3}

Table 2: Input parameters under investigation and ranges used for each in the analyses (following Feingold et al., 2016).

Given that the model output here is bounded between zero and one, some transformation may improve the fitting results. For instance, a logit-transformation might be thought to be better suited to a Gaussian model (like in Henderson et al., 2009; Andrianakis et al., 2015) or a spatial process designed to model proportions directly (Paradinas et al., 2018). Prior to fitting the partitioning models, we fitted a standard GP model to the logit-transformed output, and we found the GP performed very poorly because the step in the function is exacerbated by the transformation. We also fitted the TGP and the proposed model to the logit-transformed data and found that they both produced worse estimates than for the raw output fit. Here this can be explained by the outputs

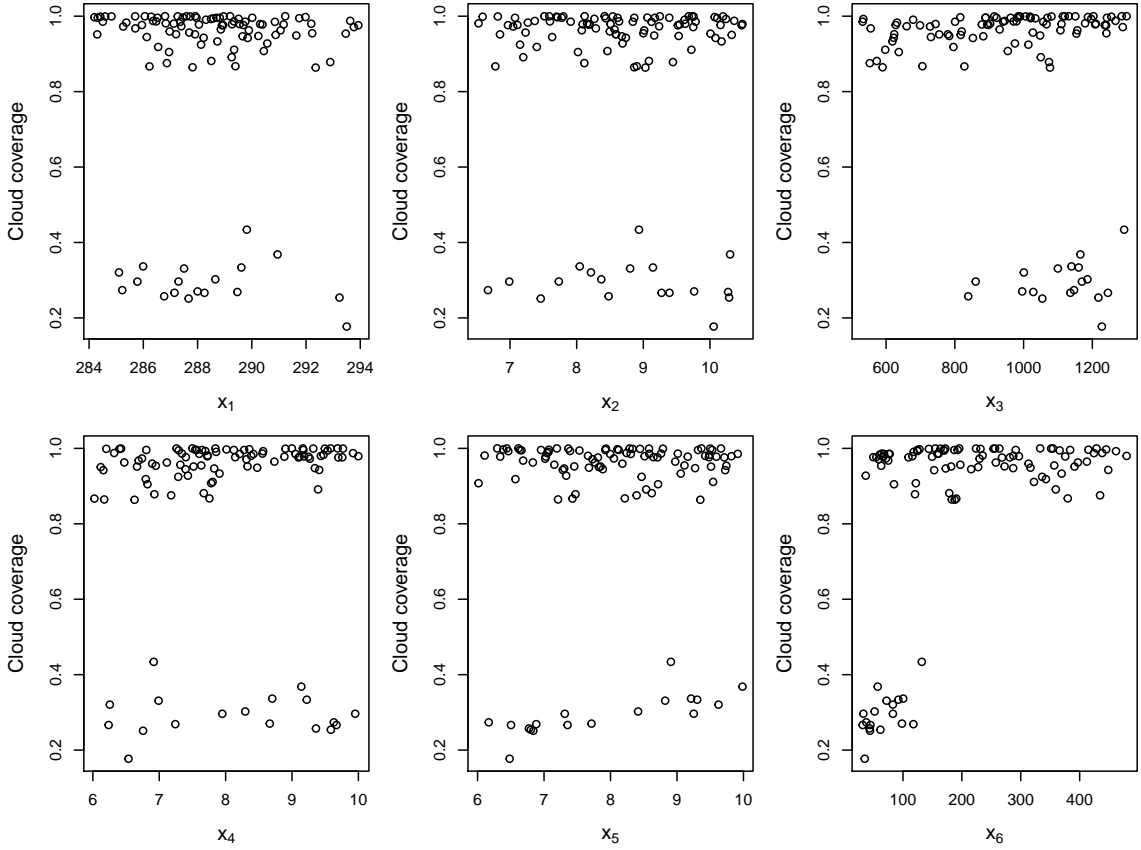


Figure 5: The scatterplots of each input plotted against the output for the original 105 cloud coverage data-points.

being at the high end of the percentage range.

The posterior sample from the proposed methodology indicates that the MAP model obtained contains two regions. The posterior distribution for the number of regions, shown in Table 3, indicates that two regions ($\Pr(r = 2|\mathbf{D}) = 0.667$) is the most probable number, despite the fact that no prior knowledge of this was incorporated.

Number of regions	1	2	3
Probability	0.102	0.667	0.231

Table 3: The posterior probability distribution for the number of regions.

A further 35 simulations with different input parameter configurations to the training data were run through the computer simulator and used for validation, following the advice of Bastos and O’Hagan (2009). The proposed method performs better at predicting these validation points ($\text{MSE} = 0.016$) than the TGP ($\text{MSE} = 0.032$) and the standard GP ($\text{MSE} = 0.025$) methods. Following this, we refitted the model using all 140 simulations as training points, and then the adaptive sampler

method from Section 4 was implemented. An additional 25 parameter combinations were selected, chosen using a candidate set of 170,000 points sampled on the boundary of the smaller (low cloud fraction) region, and these simulations were run.

The new simulations were incorporated in the training data set and the model refitted. The resulting MAP model has two regions, and the posterior sample yields $\Pr(r = 2|\mathbf{D}) = 0.87$. The MAP model has 18 Voronoi cells corresponding to one region and 87 corresponding to the other region. The region with 18 cells corresponds to low cloud fraction output and will be referred to as the smaller region. The region with 87 cells corresponds to high cloud fraction output and will be referred to as the larger region.

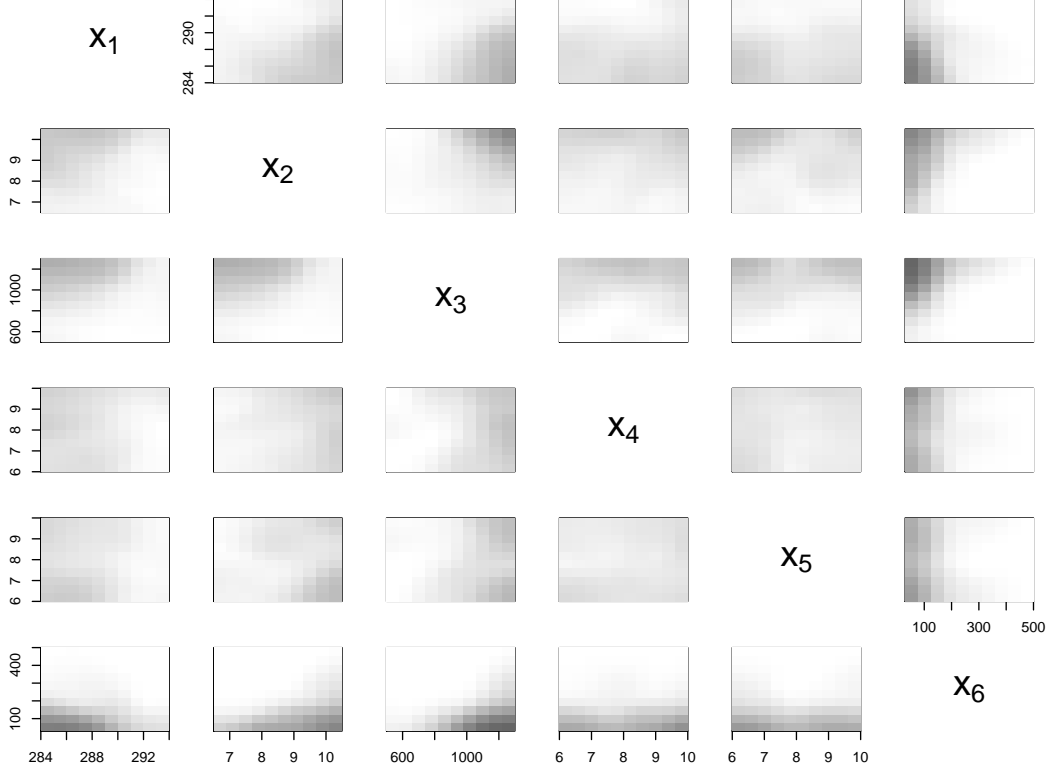


Figure 6: The ‘averaged’ proportion of points that lie within the smaller region for each of the 2-d projections based on the MAP model.

Visualising the shape of the two regions and the discontinuity between them is challenging in $d > 3$ dimensions. In Figure 6, we attempt to visualise the shape of the boundary of these regions of cloud behaviour. We used ten equispaced points in each input dimension to create a grid of 1,000,000 equispaced points over the six dimensions, and noted which points lie in each region of the MAP model. To aid with visualisation, we perform a dimension reduction technique using a 2-d averaging scheme. There are 15 possible pairwise combinations of input variables $\{(x_1, x_2), (x_1, x_3), \dots\}$, which are each assigned 100 equally spaced points in 2-d. For each of these points, there are 10,000 possible

combinations that the other inputs can take and we compute the proportion of these 10,000 points that lie within the smaller region. In Figure 6, we use a grey scale to represent this proportion, with a white or black block meaning that all of the points lie within the larger or smaller of the two regions respectively, and so correspond to areas of high or low cloud fraction output.

Figure 6 shows that the smaller (low cloud fraction) region does indeed appear to have a complex shape in the parameter space as initially suspected. In particular, an interesting aspect of this region can be seen in x_6 , the aerosol concentration. It appears that smaller values of aerosol concentration are much more likely to be attributed to the smaller region corresponding to low cloud fraction. This observation is supported by the MAP model that was seen when a TGP was attempted with the MAP model splitting the range of the aerosol concentration input variable at 117.7 cm^{-3} . Figure 6 also indicates a reason why the TGP performed poorly compared to the proposed method; in the (x_1, x_6) , (x_2, x_6) and (x_3, x_6) projections, we see that the region appears to have a curved boundary, which the TGP will not be able to model accurately with straight lines.

The results presented here show that, by using the proposed modelling approach, we are able to more clearly and accurately capture and represent the discontinuity that corresponds to the sharp change in cloud behaviour over the six-dimensional parameter space of the cloud model initial conditions. This is an important result to the cloud modelling community, as this enables the identification of the key initial conditions under which these changes in behaviour may occur. We are also able to determine the sensitivity of the cloud fraction output to the co-varying initial conditions. Full exploration of this may ultimately lead to improvements in the way the shallow cloud coverage is represented in climate models.

7 Discussion

In this paper, we developed a method that can be used to model functions that we believe contain discontinuities or display heterogeneous characteristics. The use of Voronoi tessellations as a tool to partition the input space has been shown to be advantageous over similar methods such as treed GP in the simulations and data we explored. The idea of joining Voronoi tiles is trivial to extend to other methods; for example, we could join partitions of the treed GP to create larger and non-convex regions.

There are computational benefits to the proposed approach over fitting a standard Gaussian process model: instead of fitting a Gaussian process model to n function outputs, which requires the inversion of a $n \times n$ matrix and has computing time in $\mathcal{O}(N^3)$, we fit Gaussian process models to sets of outputs that are smaller in size. For instance, if we divide \mathcal{X} into k regions, we have that the largest region could have at most $n - (k - 3)$ data points.

Standard Voronoi tessellations were used to partition the input space due to their flexibility.

However, using standard Voronoi tessellations still partitions the input space with straight lines and more flexibility over the shape of these partitions would be preferable. One possible extension is the use of weighted Voronoi tessellations. The use of weights on Voronoi tessellations allows for a greater range of partition shapes. For example, we could use multiplicatively weighted Voronoi tessellations to create round partitions or additively weighted Voronoi tessellations to create hyperbolic curves to partition the input space (Okabe et al., 2000). Another generalization is the additively weighted power diagram or sectional Voronoi tessellation (Okabe et al., 2000), formed by the intersection of the input space with a Voronoi tessellation in a higher-dimensional space. The cells of the sectional tessellation are again convex polytopes, but the configurations of cells that can occur differ from those in a standard Voronoi tessellation. Differences can be shown to occur with probability one if the higher-dimensional tessellation is Poisson-Voronoi; see Chiu et al. (1996) for a more precise statement and proof. The use of these weights however will add a new set of parameters to the model that need to be estimated and therefore increase the model complexity. Exploration is needed as to whether the increased flexibility justifies the additional computational cost. Alternatively, we can consider perturbing the individual vertices of the Voronoi cells. Again, this is computationally expensive, but it adds flexibility by allowing polygonal but non-convex cells, as used by Blackwell and Møller (2003).

The methods developed depend on forming partitions of the locations \mathbf{x}_i in order to fit separate Gaussian processes. There may be some connection to the partitions formed by mixture clustering methods, although the use of the function values y_i in allocating observations to partitions, and the disjoint nature of the regions, is rather different to conventional clustering methods.

Acknowledgements

The authors are grateful for the constructive comments of the editors and referees that have led to improvements in this paper.

References

- Abt, M. (1999). Estimating the prediction mean squared error in Gaussian stochastic processes with exponential correlation structure. *Scandinavian Journal of Statistics* 26, 563–578.
- Aigner, M. (1999). A characterization of the Bell numbers. *Discrete Mathematics* 205(1), 207–210.
- Andrianakis, I., I. R. Vernon, N. McCreesh, T. J. McKinley, J. E. Oakley, R. N. Nsubuga, M. Goldstein, and R. G. White (2015). Bayesian history matching of complex infectious disease models using emulation: a tutorial and a case study on HIV in Uganda. *PLoS computational biology* 11(1), e1003968.

- Bastos, L. S. and A. O'Hagan (2009). Diagnostics for Gaussian process emulators. *Technometrics* 51(4), 425–438.
- Blackwell, P. G. and J. Møller (2003). Bayesian analysis of deformed tessellation models. *Advances in Applied Probability* 35(1), 4–26.
- Chiu, S. N., R. Van de Weygaert, and D. Stoyan (1996). The sectional Poisson Voronoi tessellation is not a Voronoi tessellation. *Advances in Applied Probability* 28(2), 356–376.
- Cleveland, W. S., E. Grosse, and W. M. Shyu (1992). Local regression models. *Statistical Models in S* 2, 309–376.
- Conti, S. and A. O'Hagan (2010). Bayesian emulation of complex multi-output and dynamic computer models. *Journal of Statistical Planning and Inference* 140(3), 640–651.
- Cressie, N. (1993). *Statistics for Spatial Data (rev.ed.)*. New York: Wiley.
- Currin, C., T. Mitchell, M. Morris, and D. Ylvisaker (1991). Bayesian prediction of deterministic functions, with applications to the design and analysis of computer experiments. *Journal of the American Statistical Association* 86(416), 953–963.
- Feingold, G., A. McComiskey, T. Yamaguchi, J. S. Johnson, K. S. Carslaw, and K. S. Schmidt (2016). New approaches to quantifying aerosol influence on the cloud radiative effect. *Proceedings of the National Academy of Sciences* 113(21), 5812–5819.
- Fricker, T. E., J. E. Oakley, and N. M. Urban (2013). Multivariate Gaussian process emulators with nonseparable covariance structures. *Technometrics* 55(1), 47–56.
- Gallier, J. (2008). Notes on convex sets, polytopes, polyhedra, combinatorial topology, Voronoi diagrams and Delaunay triangulations. *arXiv preprint arXiv:0805.0292*.
- Giunta, A., S. Wojtkiewicz, and M. Eldred (2003). Overview of modern design of experiments methods for computational simulations. In *41st Aerospace Sciences Meeting and Exhibit*, pp. 649.
- Gramacy, R. B. and H. K. H. Lee (2008). Bayesian treed Gaussian process models with an application to computer modeling. *Journal of the American Statistical Association* 103(483), 1119–1130.
- Green, P. J. (1995). Reversible jump Markov chain Monte Carlo computation and Bayesian model determination. *Biometrika* 82(4), 711–732.
- Handcock, M. S. and M. L. Stein (1993). A Bayesian analysis of kriging. *Technometrics* 35(4), 403–410.

- Heaton, T. and B. Silverman (2008). A wavelet- or lifting-scheme-based imputation method. *Journal of the Royal Statistical Society: Series B (Statistical Methodology)* 70(3), 567–587.
- Henderson, D. A., R. J. Boys, K. J. Krishnan, C. Lawless, and D. J. Wilkinson (2009). Bayesian emulation and calibration of a stochastic computer model of mitochondrial DNA deletions in substantia nigra neurons. *Journal of the American Statistical Association* 104(485), 76–87.
- Higdon, D. (1998). A process-convolution approach to modelling temperatures in the north atlantic ocean. *Environmental and Ecological Statistics* 5(2), 173–190.
- Illian, J., A. Penttinen, H. Stoyan, and D. Stoyan (2008). *Statistical Analysis and Modelling of Spatial Point Patterns*. Chichester: John Wiley & Sons.
- Johnson, M., L. Moore, and D. Ylvisaker (1990). Minimax and maximin distance designs. *Journal of Statistical Planning and Inference* 26(2), 131 – 148.
- Khairoutdinov, M. F. and D. A. Randall (2003). Cloud resolving modeling of the ARM summer 1997 IOP: Model formulation, results, uncertainties, and sensitivities. *Journal of the Atmospheric Sciences* 60(4), 607–625.
- Kim, H., B. Mallick, and C. Holmes (2005). Analyzing nonstationary spatial data using piecewise Gaussian processes. *Journal of the American Statistical Association* 100, 653–668.
- Linkletter, C., D. Bingham, N. Hengartner, D. Higdon, and K. Q. Ye (2006). Variable selection for Gaussian process models in computer experiments. *Technometrics* 48(4), 478–490.
- Loeppky, J. L., L. M. Moore, and B. J. Williams (2010). Batch sequential designs for computer experiments. *Journal of Statistical Planning and Inference* 140(6), 1452–1464.
- Nagy, B., J. L. Loeppky, and W. J. Welch (2007). Fast Bayesian inference for Gaussian process models. Technical report, Department of Statistics, The University of British Columbia.
- Oakley, J. (2002). Eliciting Gaussian process priors for complex computer codes. *The Statistician* 51, 81–97.
- O’Hagan, A. (1992). Some Bayesian numerical analysis. In *Bayesian Statistics 4* (eds. Bernardo, J.M. et al.), pp. 345–363. Oxford: Oxford University Press.
- Okabe, A., B. Boots, K. Sugihara, and S. Chui (2000). *Spatial Tessellations: Concepts and Applications of Voronoi Diagrams*. New York: Wiley.
- Paciorek, C. J. and M. J. Schervish (2006). Spatial modelling using a new class of nonstationary covariance functions. *Environmetrics* 17(5), 483–506.

- Paradinas, I., M. G. Pennino, A. López-Quilez, M. Marin, J. M. Bellido, and D. Conesa (2018). Modelling spatially sampled proportion processes. *REVSTAT-Statistical Journal* 16(1), 71–86.
- Risser, M. D. (2016). Review: Nonstationary spatial modeling, with emphasis on process convolution and covariate-driven approaches. *arXiv preprint arXiv:1610.02447*.
- Risser, M. D. and C. A. Calder (2015). Local likelihood estimation for covariance functions with spatially-varying parameters: the convospat package for r. *arXiv preprint arXiv:1507.08613*.
- Rougier, J. (2008). Efficient emulators for multivariate deterministic functions. *Journal of Computational and Graphical Statistics* 17(4), 827–843.
- Sacks, J., W. Welch, T. Mitchell, and H. Wynn (1989). Design and analysis of computer experiments. *Statistical Science* 4, 409–423.
- Sampson, P. D. and P. Guttorp (1992). Nonparametric estimation of nonstationary spatial covariance structure. *Journal of the American Statistical Association* 87(417), 108–119.
- Santner, T., B. Williams, and W. Notz (2003). *The Design and Analysis of Computer Experiments*. New York: Springer.
- Schmidt, A. M. and A. O’Hagan (2003). Bayesian inference for non-stationary spatial covariance structure via spatial deformations. *Journal of the Royal Statistical Society: Series B (Statistical Methodology)* 65(3), 743–758.
- Williams, B. J., T. J. Santner, and W. I. Notz (2000). Sequential design of computer experiments to minimize integrated response functions. *Statistica Sinica*, 1133–1152.
- Wood, S. A., W. Jiang, and M. Tanner (2002). Bayesian mixture of splines for spatially adaptive nonparametric regression. *Biometrika* 89(3), 513–528.